Ceramics International xxx (xxxx) xxx

Contents lists available at ScienceDirect

Ceramics International

journal homepage: www.elsevier.com/locate/ceramint

Incorporation of azithromycin into akermanite-monticellite nanocomposite scaffolds: Preparation, biological properties, and drug release characteristics

M. Assarzadehgan [a], Ibrahim Saeed Gataa [b], Zainab Younus Abdullah [c], M. Kasiri-Asgarani [a,**], A. Najafinezhad [a], H.R. Bakhsheshi-Rad [a,*], M. Razzaghi [a], Soheil Salahshour [d,e,f], D. Toghraie [g]

[a] Advanced Materials Research Center, Department of Materials Engineering, Najafabad Branch, Islamic Azad University, Najafabad, Iran
[b] Warith Al-Anbiyaa University, Karbala, 56001, Iraq
[c] Department of Dental Technology, Al-Amarah University College, Maysan, Iraq
[d] Faculty of Engineering and Natural Sciences, Istanbul Okan University, Istanbul, Turkey
[e] Faculty of Engineering and Natural Sciences, Bahcesehir University, Istanbul, Turkey
[f] Department of Computer Science and Mathematics, Lebanese American University, Beirut, Lebanon
[g] Department of Mechanical Engineering, Khomeinishahr branch, Islamic Azad University, Khomeinishahr, Iran

ARTICLE INFO

Handling Editor: Dr P. Vincenzini

Keywords:
Monticellite-akermanite composite scaffold
Mechanical strength
Cytotoxicity
Antimicrobial activity
Drug delivery

ABSTRACT

Bioceramics composed of calcium and magnesium silicates have garnered increasing attention for the development of porous scaffolds in bone tissue engineering (BTE). This heightened interest is primarily attributed to their remarkable bioactivity and their capacity to form strong bonds with hard tissue. Fabricating nanocomposite scaffolds is a recognized approach for improving the characteristics of scaffolds used in BTE. This research investigates the mechanical and biological properties, antibacterial activity, and drug-release characteristics of scaffolds composed of akermanite (AKT), monticellite (MON), and monticellite-akermanite (MON-AKT). These scaffolds were fabricated utilizing the space holder process. Additionally, the *in vitro* drug release profile and antimicrobial activity of Azithromycin (AZT)-loaded MON-AKT composite scaffolds were investigated. The findings showed that the Mon-15 wt% AKT nanocomposite scaffold had the highest density, the smallest grain and micropore sizes, and the lowest porosity. In contrast, integrating AKT into MON-based composite scaffolds resulted in materials characterized by high mechanical strength and stability within physiological environments. The MON-AKT nanocomposite scaffolds exhibited cytocompatibility and demonstrated a high level of alkaline phosphatase (ALP) activity in osteogenic studies. Furthermore, antimicrobial activity assessments revealed that the AZT-encapsulated MON-AKT composite scaffolds effectively inhibited the growth of both *S. aureus* and *E. coli* bacteria. The outcomes showed that the antibacterial efficacy of the scaffold depends on both the amount of AZT and the type of bacteria. Overall, MON-AKT/3AZT scaffolds exhibited significantly superior bacterial inhibition compared to other scaffolds, making it a promising option for treating bone tissue defects.

1. Introduction

In the present era, the development of new biomaterials for bone tissue engineering (BTE) is essential, driven by the rapidly increasing need for effective treatments of bone defects [1]. Bioactive ceramics and glasses designed for bone healing encompass various materials, including titanium dioxide, Bioglass® 45S5, calcium phosphates like hydroxyapatite (HAp), and α- or β-tricalcium phosphate, as well as calcium silicates. These materials undergo modifications through doping with elements like zinc (Zn), zirconium (Zr), iron (Fe), silver (Ag), strontium (Sr), magnesium (Mg), and copper (Cu). Additionally, composite materials combining these ceramics are part of the ongoing developments in this field [2–7]. Like metallic materials, the integration of bioactive ceramics with polymers has garnered significant consideration in the construction of composite scaffolds. This approach aims to leverage the distinct advantages offered by these two diverse classes of

* Corresponding author.
** Corresponding author.
E-mail addresses: m.kasiri@pmt.iaun.ac.ir (M. Kasiri-Asgarani), rezabakhsheshi@pmt.iaun.ac.ir (H.R. Bakhsheshi-Rad).

https://doi.org/10.1016/j.ceramint.2024.08.238
Received 6 April 2024; Received in revised form 10 August 2024; Accepted 13 August 2024
Available online 15 August 2024

biomaterials [1,6,8]. Gaining prominence as a prospective alternative to bioglasses and calcium phosphates, calcium silicate-based bioceramics (CSBs) have garnered attention in the biomaterials research sphere since the mid-2000s [1,9]. However, the main limitation linked to calcium silicate, encompassing materials such as akermanite (AKT), diopside (DIO), monticellite (MON), and merwinite (MER), stems from its insufficient mechanical properties. This inadequacy hinders its potential to effectively replace either cortical or cancellous bone tissue [10–13]. Consequently, researchers have initiated the incorporation of different metal ions into the crystal structure of α-calcium silicate to create novel bioceramics with improved chemical, physical, and biological characteristics [9]. Moreover, ceramics based on nanocomposites at the nano-level exhibit intriguing functional properties attributed to their larger surface-to-volume ratio and their extremely fine structure, resembling biological apatite. These characteristics are anticipated to significantly influence the interaction between implants and cells in the body environment [7]. Furthermore, nanosized bioceramics have demonstrated superior mechanical properties and enhanced bioactivity when compared to their coarser crystal counterparts [14]. In this context, the sol-gel technique is noted for offering improved homogeneity and surface area, leading to increased dissolution. This, in turn, has the potential to enhance the bioactivity of the bioceramic and lower the preparation temperature [15,16]. Furthermore, the sol-gel method is recognized as a versatile process for producing fine powders that could be easily sintered, allowing for the formation of various forms such as dense, porous, fiber, and film structures [16,17]. Fortunately, prior research indicates that bioactive ceramics like MON, with the chemical formula of $CaMgSiO_4$, possess significant potential for utilization in bone healing, given their closer Young's modulus to cortical bone, and superior fracture toughness, compared to HAp, and outstanding bioactivity stemming from the dissolution of Ca, Si, and Mg ions [15]. Nevertheless, MON exhibits low fracture toughness, restricting its application in load-bearing tissue regeneration [11]. Therefore, it is imperative to enhance its mechanical properties through composite preparation, involving the combination of materials composed of two or more basic components, each contributing preferred properties and mitigating the limitations of individual components [15]. AKT, with the chemical formula of $CaMgSi_2O_6$, is osteogenically active and possesses superior mechanical properties compared to other micro-/-nanostructured composites based on calcium phosphate [18,19]. Additionally, AKT demonstrates good stability in terms of degradation rate, which is a critical characteristic for scaffold design and bone regeneration [18]. Previous studies have shown that the alkaline ions Ca^{2+}, Mg^{2+}, and Si^{4+} released from akermanite dissolution significantly promote the proliferation of mouse fibroblast L929 cells [19–22]. Nevertheless, MON-AKT scaffolds exhibited inadequate antibacterial performance, leading to implants being susceptible to infections and contributing to postoperative complications [23,24]. Bacterial infections involving *Staphylococcus epidermidis*, *Escherichia coli (E.coli)*, *Staphylococcus aureus (S. aureus)*, and *Pseudomonas aeruginosa* are prevalent, primarily due to the ease with which these bacteria can adhere to the bone matrix [25,26]. Bone defects affected by infections manifest as prolonged situations where the regenerative potential of nearby tissues and bones is substantially hindered by pathogenic infections. Addressing this issue is a major challenge in orthopedic care and for orthopedic surgeons [23,27]. Open fractures, blood transmission from adjacent regions, or the presence of implants can facilitate the dissemination of infections. Overactive inflammatory reactions impede the regeneration of bone tissue, resulting in substantial disruptions to the healing process of bone [28]. Therefore, the antibacterial properties of bioceramics play a crucial role in overcoming prevalent microbial infections that may affect bone implants [19,28]. An effective method involves loading and/or implanting antibiotics to prevent bone infections and expedite the bone healing process [28,29]. Azithromycin (AZT) functions as an antibacterial agent in human medical applications, utilized to address or prevent diverse health conditions such as pharyngitis, pneumonia, persistent bronchitis, bronchopneumonia, infections affecting the skin and soft tissues, and specific sexually transmitted diseases [21,25]. Due to its widespread use in treating infections, it is crucial to identify the optimal concentration of AZT to maximize effectiveness and avoid toxicity [26,30]. To our knowledge, research on nanocomposite MON-AKT scaffolds infused with antibiotics to enhance bone scaffold effectiveness is limited. The study aims to synthesize high-purity MON and AKT, and subsequently, MON-AKT-based nanocomposite scaffolds using a combination of ball milling and sol-gel methods. This research investigates the bio-mineralization mechanisms, including apatite deposition and dissolution behavior, as well as the mechanical properties and biodegradability in simulated body fluid (SBF) for the three designated ceramics. In this context, MON-AKT bioceramic scaffolds are loaded with varying concentrations of AZT to assess the drug release behavior and antibacterial properties of AZT-encapsulated nanocomposites. In conclusion, this study aims to evaluate the effectiveness of AZT-loaded MON-AKT scaffolds in regenerating bone defects and managing bone infections.

2. Experimental procedures

2.1. Preparation of Mon-AKT scaffolds loaded with AZT

MON ($CaMgSiO_4$) ceramic powders were produced using the sol-gel synthesis approach. The raw materials, including calcium nitrate tetrahydrate ($Ca(NO_3)_2{\cdot}4H_2O$), magnesium nitrate hexahydrate ($Mg(NO_3)_2{\cdot}6H_2O$), and tetraethyl orthosilicate ($Si(OC_2H_5)_4$, TEOS), were mixed in a molar ratio of 1:1:1. The process initiated by mixing TEOS with deionized (DI) water and a catalyzing agent, HNO_3 solution (2 N). Sequentially, calcium nitrate tetrahydrate and magnesium nitrate hexahydrate were gradually added over 1-h intervals with continuous stirring. After the reaction, the transparent sol was sealed and left to age at 60 °C. The resulting gel was dried, then ball milled and calcined at 1100 °C for 2 h to obtain MON particles, which exhibited sizes between 38 and 74 μm [31]. The substances underwent milling in zirconia vials with zirconia balls using a PM 400-Reutch planetary ball mill for a duration of 3 h. During ball milling, the ball-to-powder weight ratio was maintained at 10:1, with a deionized water-to-powder ratio of 3:1 and a vial speed fixed at 500 rpm. The scaffolds were fabricated employing the space holder process. Briefly, MON powder was blended with various amounts of AKT powder, including 15 wt%. AKT was synthesized under stoichiometric conditions using the previously described method, with the only variation being the molar ratios of calcium oxide, magnesium oxide, and silicon dioxide. MON ($CaMgSiO_4$) and AKT ($Ca_2MgSi_2O_7$) were produced with molar ratios of 1:1:1 and 2:1:2 for calcium oxide, magnesium oxide, and silicon dioxide, respectively. Next, NaCl with a particle size of 300–500 μm, used as a spacer, was mixed with the previously prepared MON-AKT nanopowder blend in a weight ratio of 75 %–25 %. The resultant mixed powder underwent compression under 110 MPa, using a cylindrical-shaped mold, to make cylinders with Φ10 mm *15 mm, or Φ16 mm*9 mm dimensions. NaCl particles were then removed by immersing the specimens in distilled water for 24 h. To fully remove the NaCl particles, the cylinders were sintered at 1300 °C for 4 h, with a heating rate of 5 °C/min. Subsequently, different concentrations of AZT solution, including 1, 3, and 7 mg/mL, were prepared by dissolving the required AZT powder in distilled water. The loading procedure involved subjecting each MON-AKT scaffold to a 5-min vacuum before immersing it in the prepared AZT solutions. Subsequently, the resulting scaffold samples with different concentrations of AZT, denoting MON-AKT/1AZT, MON-AKT/3AZT, and MON-AKT/7AZT, underwent agitation on a roller shaker for 24 h and were then dried overnight in an oven. Fig. 1 illustrates this approach schematically. Interconnected and total porosity were determined using Archimedes' principle. Total porosity included both interconnected and closed pores as calculated by:

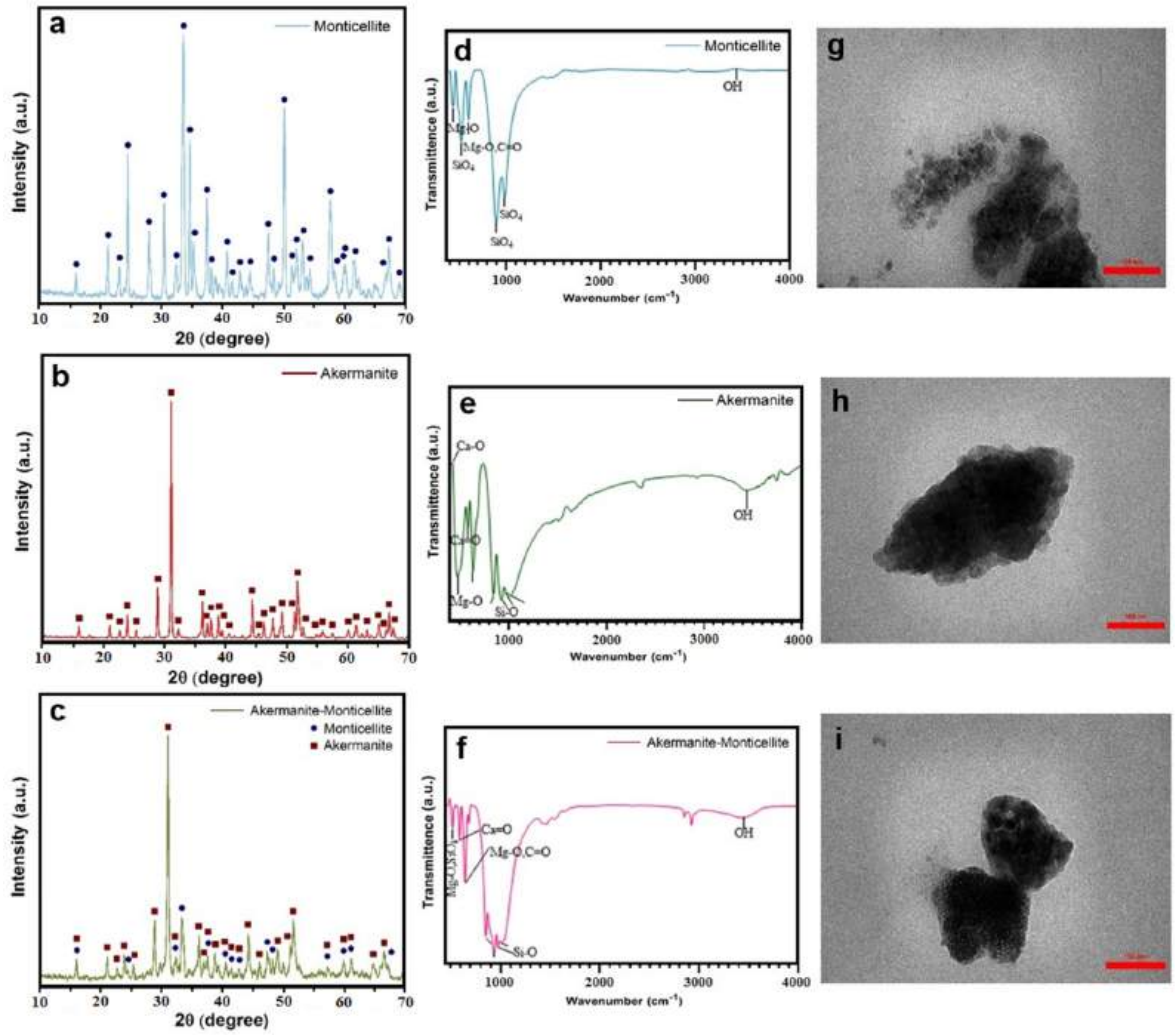

Fig. 1. (a–c) XRD pattern, (d–f) FTIR spectrum, and (g–i) TEM image of MON, AKT, and MON-AKT scaffold samples.

$$\text{Total porosity} = 1 - \frac{Wd}{\rho(\text{wd} - \text{Ws})} \times 100 \quad (1)$$

where W_d is the weight of the sample in air, W_s is the weight of the sample suspended in water, and ρ is the true density of the MON-AKT material.

2.2. Characterization of microstructure

Fourier transform infrared (FTIR) spectroscopy was utilized to characterize the functional groups within MON, AKT, AZT, and MON-AKT/AZT scaffolds. The FTIR spectra were obtained within the spectral range of 4000 to 450 cm^{-1} to identify specific functional groups. The microstructures of the scaffold samples were examined using a Hitachi HT7700 transmission electron microscope (TEM) and a JEOL JSM-6380LA scanning electron microscope (SEM), both equipped with JEOL energy dispersive X-ray spectroscopy (EDS) technology. All mentioned equipment was made in Japan. Furthermore, phase components were identified using a Siemens D5000 X-ray diffractometer with Cu-Kα radiation (45 kV, 40 mA). The diffraction angles (2θ) were scanned from 20 to 80° at a speed of 4° per minute. The crystallite size was determined using the Williamson–Hall method, expressed as:

$$\frac{\beta}{2}\cot\theta = \frac{0.45\lambda}{\text{Sin}\theta D} + \varepsilon \quad (2)$$

In this context, β represents the width of the diffraction peak at its mid-height, λ signifies the X-ray wavelength, and D denotes the average crystallite size in nanometers (nm). Also, the microstrain and Bragg diffraction angle are indicated in the formula by ε and θ, respectively. The compressive characteristics of cylindrical-shaped sintered MON-AKT scaffolds, with Φ 6 × 9 mm^2 dimensions, were assessed at ambient temperature following ASTM-E9-09 standards. An STM-50 SANTAM universal testing machine was employed, maintaining a constant crosshead speed of 0.5 mm/min to achieve a strain rate of 0.006 s^{-1} for the specimens. Stress-strain curves were recorded and analyzed to determine compressive strengths.

2.3. In vitro bioactivity and biocompatibility

To investigate the bioactivity *in vitro*, first, the MON, AKT, and MON-AKT scaffold specimens were immersed in 100 mL of SBF solution, prepared based on the Kokubo protocol [32], at 36.5 ± 1 °C for 28 days. After the 28-day soaking period, the specimens were washed with DI water and dried in air at ambient conditions. The identification of bone-like apatite formation on the scaffold samples was ascertained via SEM imaging, XRD, and FTIR analysis. The pH values of the solutions were continuously monitored using a Metrohm (Germany) pH meter during the entire incubation period. Additionally, the concentration of ions of corrosion products in the SBF solution, such as Ca, Mg, P, and Si was determined after a 28-day incubation period, employing inductively

coupled plasma (ICP) atomic emission spectroscopy. The assessment of biocompatibility or cytotoxicity was performed employing the 3-(4, 5-dimethylthiazol-2-yl)-2,5-diphenyltetrazolium bromide (MTT) assay. The polished samples underwent sterilization with isopropanol and ultraviolet (UV) rays. After sterilization, the specimens were immersed in the culture media for 24 h at 37 °C, and an extraction media was prepared. MG-63 cells were then seeded in 96-well culture plates at a concentration of 10^4 cells/mL of media in each well. The plates were incubated at 37 °C for 24 h and 48 h in a humidified atmosphere having 5 % CO_2, based on the procedure described in Ref. [33]. The capacity for cell differentiation was assessed by measurement of the alkaline phosphatase (ALP) activity of MG-63 cells in extracts taken at 3 and 7 days post-culture. After rinsing three times with a PBS solution, the cultured cells were treated with 0.25 % trypsin solution. Subsequently, the cells were fixed for 30 min with 4 % paraformaldehyde. Finally, the cells were stained utilizing ALP staining reagents and examined under a microscope to analyze their differentiation.

2.4. In vitro antibacterial activity and drug release evaluation

For *in vitro* investigation of AZT release, MON-AKT/AZT scaffold specimens were soaked in phosphate-buffered saline (PBS) solution and subjected to incubation at 37 °C. At designated time points, 1 mL of the PBS solution containing the discharged MON-AKT/AZT was gathered, and fresh PBS was replaced. The assessment of AZT release from the MON-AKT/AZT scaffolds was conducted at 230 nm utilizing a UV–Vis spectrophotometer. To evaluate the antibacterial properties of the MON-AKT/AZT scaffold samples against both Gram-negative *E. coli* (ATCC® 19637™) bacteria and Gram-positive *S. aureus* (ATCC® 12600™), disc diffusion antibiotic sensitivity tests were conducted based on Ref. [34].

2.5. Statistical analysis

Statistical analysis was conducted utilizing one-way ANOVA to evaluate the significance of differences in the outcomes, with a significance level set at $*p < 0.05$.

3. Results and discussion

3.1. Characterization

Fig. 1a displays the XRD pattern of the ceramic in its as-prepared state, with an examination revealing the pure crystal phase of $CaMgSiO_4$ (JCPDS 11–0353). Notably, the distinct sharp peaks and minimal background signal indicate the highly crystalline nature of the obtained $CaMgSiO_4$ ceramic [14,20,31]. Likewise, the XRD patterns of the specimen align with AKT ($CaMgSi_2O_6$) (JCPDS data file 00-035-0592) and reveal a prominent peak at approximately 31.42°, signifying the formation of a single phase as shown in Fig. 1b. As per the Williamson-Hall equation, the crystallite size of MON and AKT powders are estimated to be around 50 ± 5 and 55 ± 5 nm, respectively, following the process of milling. The mean crystallite size of MON was marginally smaller than that of AKT across all samples. No chemical reaction occurred between the spacer and the initial powders, with no new phase detected. To ensure the thorough removal of the spacer, a sintering temperature of 1300 °C was employed. In another study focusing on the *in-situ* synthesis of bioceramic nanocomposites, it was observed that, for all calcination temperatures, an increase in mechanical activation (MA) time led to a reduction in the mean crystallite sizes of the AKT and MON phases in all samples. This is attributed to the MA process, which generated elevated strain and stress values [18]. In the case of the MON-AKT composite, apart from MON as the predominant phase, AKT, which shares a similar composition to MON, was also identified at 2θ angles of 29.24°, 31.42°, 36.55°, 44.68°, and 52.12° as a minor phase, confirming the formation of the nanocomposite as shown in Fig. 1c. No other anticipated impurities, such as merwinite and diopside, were present in the samples. Fig. 1d illustrates **the FTIR spectra** of MON, AKT, and MON-AKT scaffold samples. In Fig. 4, the infrared spectra exhibit unique characteristics of MON, showcasing an absorption band at 475 cm^{-1} linked to the Mg–O bond. Clear peaks associated with Si–O bands in the SiO_4 tetrahedron affirm the formation of MON. Stretching of SiO_4 is evident in peaks at 1100–1000 cm^{-1}, 960 cm^{-1}, and 873 cm^{-1}, while bending of SiO_4 and Ca–O stretching are denoted by peaks at 616 and 530 cm^{-1}, respectively [35]. Examining the FTIR spectra of the sintered AKT specimens (Fig. 1e) reveals conspicuous bending modes at 430 cm^{-1} and 511 cm^{-1} for O–Ca–O and O–Mg–O, respectively. The peak of the Ca=O group is identifiable at 595 cm^{-1}, and the stretching modes of the Si–O group exhibit peaks within the range of 831 cm^{-1} to 929 cm^{-1}. Moreover, the symmetric stretching vibration modes of Si–O–Si and O–Si–O groups manifest at 1020 cm^{-1} and 638 cm^{-1}, respectively [19,20]. The extensive moisture adsorption detected at 3439 cm^{-1} was related to the presence of the OH– group [20,36,37]. In the FTIR spectra of the MON-AKT scaffolds, peaks associated with both AKT and MON phases were observed, and no additional peaks were detected in the composite scaffolds as shown in Fig. 1f. The TEM images in Fig. 2g–i show that all three samples exhibited a spherical morphology, including elongated spheres, characterized by a grain size less than 70 nm and a propensity to cluster together.

When designing an ideal scaffold for effective bone tissue regeneration, structural features like porosity, pore size, pore interconnectivity, and surface topology must be meticulously considered. The microstructure of MON, AKT, and MON-AKT scaffold samples is shown in Fig. 2, where the scaffold sintered at 1300 °C exhibits a porous structure predominantly ranging from 600 to 800 μm. The presence of pores on the surface of MON, AKT, and MON-AKT is attributed to the release of NaCl spacer materials during the leaching and sintering process. The interaction of bioceramic implants with surrounding tissues is significantly influenced by the presence of a porous and agglomerated surface [9,36,38]. The SEM images depict a porous structure with a high level of interconnectedness, a beneficial characteristic that enables efficient pathways for nutrient transport and waste elimination. Moreover, this porous arrangement facilitates the infiltration of bone tissue. The scaffolds did not undergo complete sintering. Alongside the specified pore size range of 600–800 μm, there was a notable quantity of smaller pores within the 2–10 μm range. Notably, the creation of the nanocomposite prevented particle enlargement, leading to a reduction in the size of pores exhibiting a honeycomb structure, as illustrated in Fig. 2. The outcomes indicate that the semi-spherical MON-AKT nanocomposite scaffolds were more distinct and a little smaller compared to the MON and AKT scaffolds. Nonetheless, sintering resulted in agglomeration across all specimens, resulting in irregular forms, particularly within the doped categories [1,9]. The formation of substantial agglomerates ensued from the existence of surface energy and the inclination of MON, AKT, and MON-AKT nanoparticles to adhere. The average grain sizes of the samples, measured from SEM images, decreased from 124.05 ± 8.21 nm for MON-AKT to 115.38 ± 11.64 nm for MON and 108.38 ± 11.64 nm for AKT. It's noteworthy that the irregularity of grains and clustering increases in MON-AKT, resulting in particles with irregular and tightly packed clustered structures. Images with high magnification confirmed the formation of interconnected pores, which are homogeneously distributed throughout the samples as shown in Fig. 3a–c. These micropores are required to create a conducive environment for bone tissue growth and fluid exchange within the body [31,39]. The existence of micro and macro pores, most likely formed during the process of sintering. Since the sintering temperature of the scaffolds (1300 °C) was close to the melting point of AKT, the AKT nanopowder functioned as a sintering agent, preventing grain growth in the MON matrix. Additionally, the ultrafine nature of the AKT powder could enhance the sintering behavior of the scaffolds because of the high energy and interfacial area density retained at the interfaces [31,40,41]. In another study [42], the influence of bioglass on the sintering behavior of HA was investigated. The findings of this study also demonstrated that bioglass remarkably

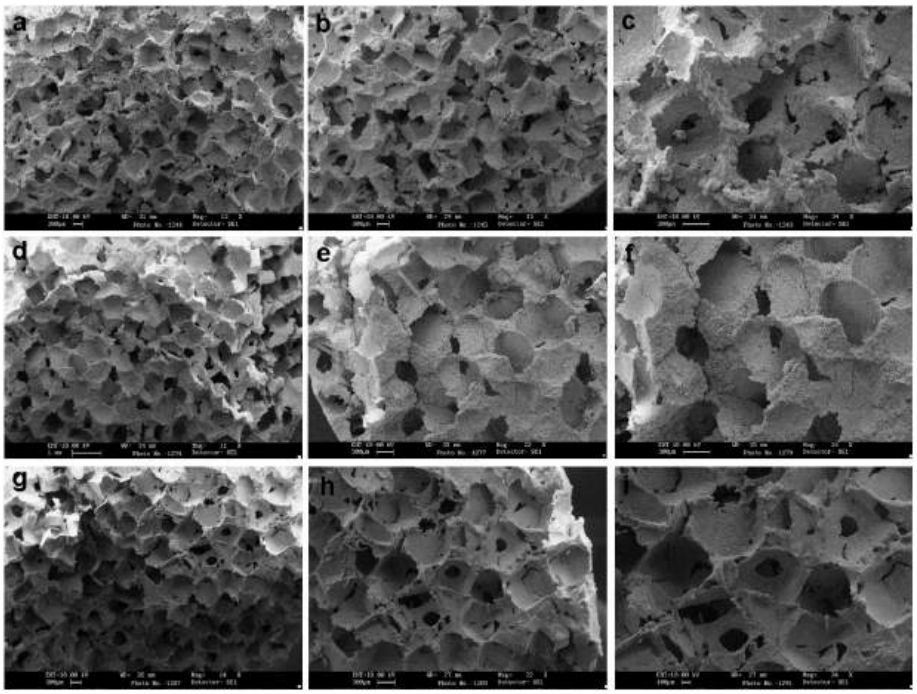

Fig. 2. SEM images of (a–c) MON scaffold (d–f) AKT scaffold and (g–i) MON-AKT composite scaffold sample.

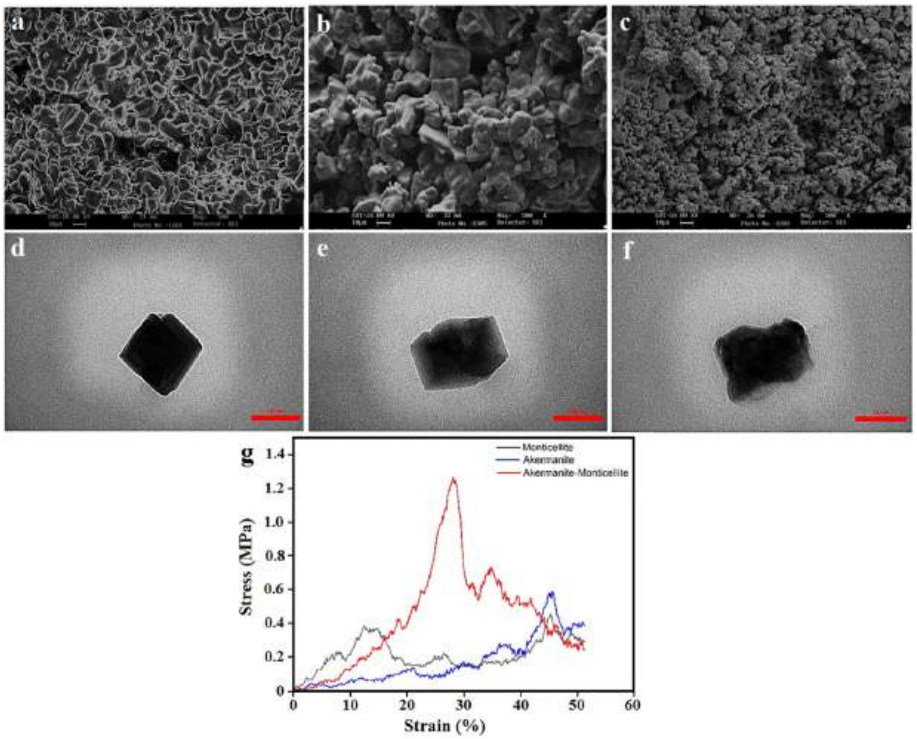

Fig. 3. High magnification SEM images of (a) MON scaffold (b) AKT scaffold and (c) MON-AKT composite scaffold sample, and TEM image of (d) MON, (e) AKT, and (f) MON-AKT composite scaffold and (g) Compressive stress-strain curves for MON, AKT, and MON-AKT scaffold samples.

hindered the grain growth of HA and can serve as an effective sintering aid. Based on our findings, MON-15 wt% AKT exhibited the highest density, the smallest grain and micropore sizes, and the lowest porosity. The grain sizes of the MON-AKT composite scaffold were approximately 1–2 μm, and a certain amount of pores was detected. As can be seen in the TEM images (Fig. 3d–f), while the MON and AKT powder consisted of cubic and semi-like cubic particles with a mean size of 90 ± 2 nm and 100 ± 5 nm, the particles of Mon- AKT were irregular in shape with the mean size of 65 ± 3 nm. The average particle size of the scaffolds in different scaffolds further confirmed the effects of AKT on the suppression of grain growth. With the addition of the 15 wt% AKT into the MON-based scaffold the particle size of the composite scaffolds significantly decreased and densification improved.

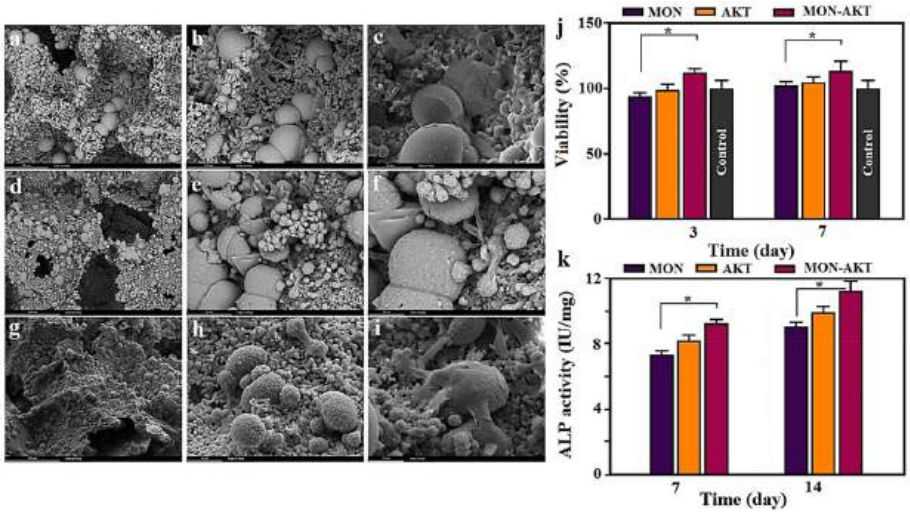

Fig. 4. SEM images of the morphology and adhesion of MG63 osteoblast cells for (a–c) MON scaffold, (d–f) AKT scaffold and (g–i) MON-AKT composite scaffold sample, (j) Viability of MG63 osteoblast cells and (k) ALP activity of MG63 osteoblast cells cultured for various durations on MON, AKT, and MON-AKT scaffold samples (*$p < 0.05$).

3.2. Mechanical properties evaluation

Scaffolds designed for application in the regeneration of bone tissue should exhibit mechanical characteristics that are similar to the natural properties of the host bone. Moreover, biofabricated scaffolds are expected to function as provisional structures until the complete maturation of the tissue occurs [9,36]. Converting a novel nanostructured bioceramic into a bone scaffold in the initial stages necessitates the simultaneous achievement of favorable mechanical characteristics and interconnected macroporosity. It is widely recognized that, typically, ceramics must undergo sintering at temperatures exceeding 1000 °C to achieve the requisite mechanical strength suitable for applications involving bearing loads. Therefore, optimizing a ceramic scaffold to achieve both desirable mechanical characteristics and porosity is of paramount importance [9]. Compressive stress-strain curves for MON, AKT, and MON-AKT scaffold samples are exhibited in Fig. 3g. The compressive strength of the MON scaffold and AKT scaffold was 0.39 ± 0.03 MPa, and 0.58 ± 0.03 MPa, respectively; it increased to, 1.27 ± 0.3 MPa for MON-AKT. The findings suggested that the mechanical characteristics of the porous ceramics produced were significantly impacted by the solid content, resulting in varied porosity and pore structures. Augmented porosity and larger pore dimensions adversely affect compressive strength, while a singular circular pore structure would enhance mechanical properties. The compressive strength showed significant differences among all groups. Among the monolithic ceramic scaffold samples, AKT specimens exhibited a higher compression strength. Akermanite is tetragonal, while MON is octahedral. Discrepancies in the structural dimensionality of the silicates are probable contributors to differences in both degradation behavior and mechanical strength [3]. The compacted MON-AKT scaffolds, fabricated from nanocomposite powder and sintered at 1300 °C for 3 h, demonstrated remarkable enhancements in mechanical characteristics compared to pure MON and AKT scaffolds. This enhancement positions it as an appropriate candidate for use in BTE purposes. A nanosized structural composite with lower porosity and higher densifications can create characteristics for a high specific surface area, resulting in increased mechanical properties [43]. According to our data, the incorporation of AKT into the MON scaffold, creating scaffolds composed of two phases, leads to an enhancement in the mechanical properties of the scaffold samples. In this respect, it was illustrated [44] that introducing an insignificant content of CaF_2 improved the composite mechanical characteristics by making the composite denser and reducing the number of pores significantly. Moreover, the findings suggest that introducing a secondary phase hinders the enlargement of grains in the sintering process. The well-established Hall-Petch equation, commonly applied to explain the correlation between the grain size and yield strength in alloys and compounds, supports the notion that scaffold strength enhances as the grain size decreases.

3.3. Cell adhesion

Fig. 4a–i depict the morphology of MG-63 cells cultured on the pure MON and AKT scaffold samples, as well as the MON-AKT composite scaffold samples following 24 and 72 h of incubation. On the two monolithic MON and AKT scaffold samples, the cells appeared flat and spread with extensions. Cell attachment and spreading on the MON-AKT composite scaffold samples were more extended and uniform than on the monolithic ones as exhibited in the supporting information (Fig. A1). On the surface of the MON-AKT composite scaffolds, some cytoplasmic bridges of MG-63 cells are also observed. This implies that integrating AKT into MON scaffolds improves cell adhesion, a topic that can be explored from various perspectives. The release of ions coupled with surface reactions can positively affect protein adsorption and, consequently, cell adhesion during the incubation stage. This can be considered a positive contribution of AKT to cell adhesion. The enhancement in the apatite-formation ability of MON-AKT composite scaffolds, as observed from SEM results, can also promote protein adsorption and, consequently, cell adhesion. This is attributed to the desirable biocompatibility characteristics of apatite [3,45]. Previous studies have reported that Mg^{2+} and Si^{4+} ions can enhance the proliferation and differentiation of osteoblast cells [9]. **The MTT assay** directly reflects cell activity and viability. In general, cells exhibit metabolic activity when in direct interaction with the densely sintered specimens achieved through sintering at 1300 °C (Fig. 4j). In terms of pure scaffolds, MG63 cells cultured in AKT scaffolds demonstrated higher viability compared to those cultured in MON scaffolds. Compared to the pure MON and AKT scaffolds, the MON-AKT composite scaffolds revealed remarkably higher cell viability at every measured interval, with *$p < 0.05$. It has been demonstrated that the chemical composition of biomaterials can markedly influence cell responses. Moreover, cell viability is largely influenced by ionic dissociation products from the biomaterials. Previous studies have revealed that ionic dissociation products, like Ca^{2+}, play a vital role in stimulating the attachment and proliferation of human bone-derived mesenchymal stem cells [46]. The significance of

interactions between the substrate and cells in influencing cell growth and activity is well-acknowledged [47]. During the initial phases of attachment and proliferation of bone cells, the interaction between cells and biomaterials *in vitro* can be impacted by the size of the grains. Previous reports [46] have indicated that the reduction in grain size positively influences cell proliferation and adhesion, potentially attributed to the improved wettability playing a pivotal role in cell-biomaterial interaction in finer grain sizes. In the current investigation, the MON-AKT composite scaffolds demonstrated a finer grain size and lower apparent activation energy for grain growth compared to pure MON and AKT. This characteristic may contribute to the heightened cell viability observed across all culture periods, implying advantageous surface properties for bone cell growth. Fig. 4k displays the **ALP activity** of MG-63 cells exposed to extracts of pure and composite scaffolds at different concentrations for 3 and 7 days. A Ca-silicate-based effect on the ceramic bioactivity was demonstrated. Cells cultured on all MON, AKT, and MON-AKT scaffolds for 7 days exhibited significantly higher ALP activity than the pure MON and AKT scaffolds. In this situation, a remarkable difference in ALP activity between the pure MON scaffold and the MON-AKT scaffold was observed (*$p < 0.05$). The ALP activity of cells on all MON, AKT, and MON-AKT scaffolds notably increased with the extended culture time in the scaffolds. Among the pure scaffolds, AKT exhibited higher ALP levels than the MON scaffold. These comparative results revealed that the ALP expression level of cells exposed to MON-AKT composite scaffold extract was remarkably higher after 7 days of cell culture than other pure scaffolds. This suggests that an adequate release of bioactive ions, such as Si^{2+} and Mg^{2+}, occurred from this ceramic composite scaffold [3,48].

To assess the osteogenic differentiation of MG63 cells in contact with the specimens, **Alizarin red** staining was employed [3,48]. As depicted in Fig. 5a–c, red dots indicative of calcium deposits on the cell-seeded scaffold samples were distributed across the scaffold surface, with their intensity and density varying based on culture time and scaffold composition. Among the monolithic scaffolds, the AKT scaffold showed more calcium deposition compared to the MON scaffold. However, the MON-AKT composite scaffolds had the highest calcium deposition overall (*$p < 0.05$). It was evident that the density of these dots remarkably increased with prolonged culture time, with these changes being more pronounced on the MON-AKT composite scaffold samples. The staining data, quantitatively displayed in Fig. 5d, clearly illustrate the significant creation of calcium crystals on the MON, AKT, and MON-AKT scaffolds. These findings particularly demonstrated the remarkable potential of the MON-AKT composite scaffold for the generation of fresh bone and BTE purposes. It was shown that the ceramics absorbed varying amounts of phosphorus, which is crucial for cellular structure and function. Recent evidence has shown that the entry of phosphorus into osteoblasts via a sodium-dependent phosphate cotransporter mechanism initiates the synthesis of osteopontin mRNA and protein, consequently influencing mineralization [3]. Additionally, diverse ceramics release different quantities of essential elements like calcium, magnesium, and silicon, which play pivotal roles in gene transcription during osteogenesis. Specifically, calcium is crucial in the bone mineralization process.

3.4. *In vitro bioactivity study*

The *in vitro* bioactivity was assessed to examine the biomaterials' ability for in-vivo bone formation. Over a 28-day immersion period in SBF, the formation of an HAp layer on the sample surfaces was analyzed. The presence of HAp is crucial for the integration of bioactive materials with neighboring tissues, facilitating the combination of bone tissue with biomaterials. The evaluation of HAp formation over the surfaces of MON, AKT, and MON-AKT composite scaffolds during SBF immersion was conducted using FTIR, XRD, and SEM coupled with EDS. The SBF method, commonly employed for in-vitro bioactivity assessment, involves immersion in SBF and subsequent analysis [49]. The SEM images (Fig. 6a–f) of the MON, AKT, and MON-AKT scaffold samples soaked in SBF show the deposition of spherical bead-like particles on the surface of both pure and composite scaffolds. The deposition of HAp particles with different magnification is exhibited in the supporting information (Fig. A2). EDS analysis indicates the elemental composition of the deposited HAp on the scaffold surface, with the existence of calcium,

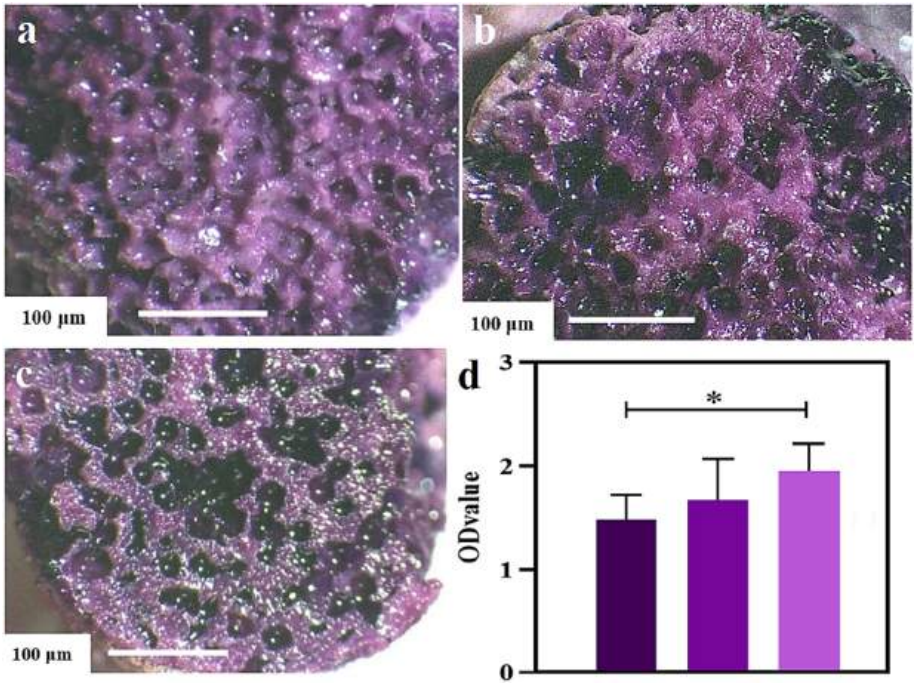

Fig. 5. Alizarin red staining of MG-63 cells cultured on (a) MON scaffold (b) AKT scaffold and (c) MON-AKT composite scaffold sample and (**d**) OD values of MON, AKT, and MON-AKT scaffold samples (*$p < 0.05$). (For interpretation of the references to colour in this figure legend, the reader is referred to the Web version of this article.)

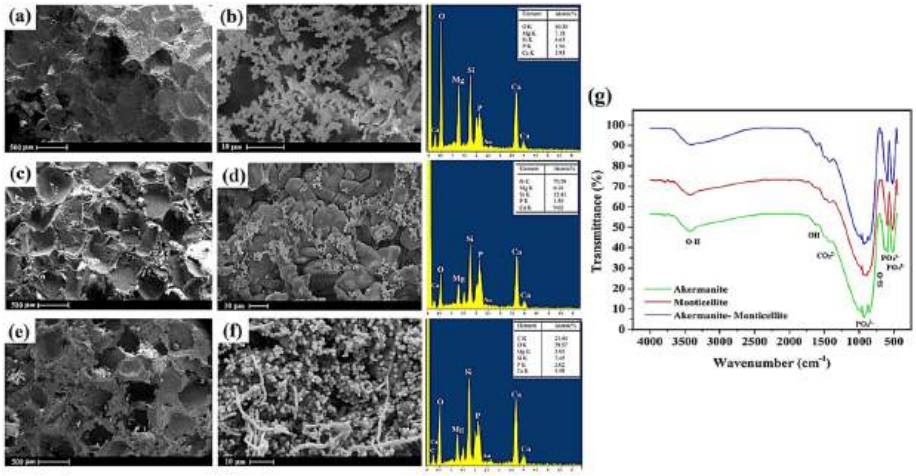

Fig. 6. SEM images of (a,b) MON scaffolds, (c,d) AKT scaffold, and (e,f) MON-AKT composite scaffold along with EDX analysis after 28-day soaking in SBF at various magnifications, and (g) FTIR absorption spectra of MON, AKT, and MON-AKT scaffold samples after 28-day soaking in SBF.

phosphorus, and oxygen, providing further evidence of HAp deposition on both the pure and composite scaffolds. The HAp formation on MON-AKT composite scaffolds is regulated by the ion exchange mechanism between Ca-silicates and the SBF. The release of calcium (Ca), silicon (Si), and magnesium (Mg) ions from the scaffold into the SBF, coupled with the incorporation of these ions into the apatite deposits, enhances the chemical stability of apatite against dissolution, thereby promoting bioactivity [50]. Initially, the Mg–O and Ca–O bonds in silicates undergo a reaction with H+ or H_3O^+ in the solution. The Mg–O bond exhibits greater strength than the Ca–O bond, attributed to its smaller ionic radius, making the dissolution of Mg ions more challenging. Following this, the Si–O on the surface forms an amorphous silica-rich layer with a negative charge, attracting dissolved Ca^{2+} ions from silicates and intrinsic cations in the saline solution [48,50]. After 28 days of immersion, the apatite phase predominantly covered the scaffold surface, with MON and AKT present as minor phases. The relatively slow rate of apatite deposition could be attributed to the existence of Mg and the micrometer-sized particle, limiting the activity to some extent. The findings suggest that MON-AKT composite scaffolds exhibited superior apatite formation in SBF compared to pure MON and AKT scaffolds immersed in SBF. Additionally, EDS analysis verified the formation of apatite after immersion. The surfaces exhibited different levels of Ca and P after soaking in SBF. Moreover, the consistent presence of P indicated that apatite formation occurred on the scaffold surface. Previous studies have indicated that Ca, Si, and Mg ions play a remarkable role in accelerating the formation of vascular channels in bone tissue [18]. The **FTIR spectrum** indicates the existence of phosphate and carbonate functional groups as presented in Fig. 6g. The absorbance bands at 485 cm^{-1}, 514 cm^{-1}, and 592 cm^{-1} are attributed to the bending vibrations of the phosphate group while stretching vibrations are observed at 980 cm^{-1} and 1027 cm^{-1}. The peaks at 1432 cm^{-1} and 1642 cm^{-1} are assigned to the CO_3^{2-} and OH groups [22,51]. Hence, the FTIR findings underscore the *in vitro* growth of bone-like apatite with enhanced growth ability, without exerting any negative impact on chemical stability.

Fig. 7a displays elemental mapping images of the MON-AKT

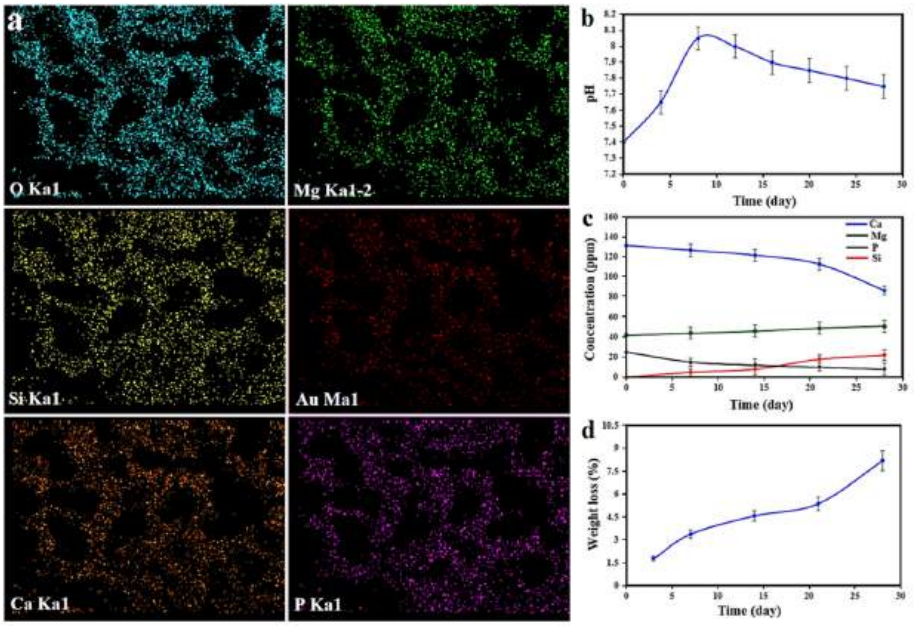

Fig. 7. (a) EDS-MAP analysis of MON-AKT composite scaffold, (b) changes of pH in the SBF solution, (c) changes in the concentration of the ions in the SBF solution, and (d) weight loss of MON-AKT composite scaffold after soaking in PBS solution.

nanocomposite scaffold, which reveal the existence and homogeneous dispersion of all of its components, assisting in visualizing and verifying their presence. The image also displayed structural characteristics that are important for bone tissue regeneration, such as the level of porosity, pore size, and level of pore interconnectivity. Fig. 7b illustrates the pH **variation** of the SBF in contact with the scaffold samples. In the case of MON-AKT composite scaffolds, the initial sharp increase over time is attributed to the exchange of bioceramic cations—especially Ca—with H^+ or H_3O^+ from the SBF. After the fourth day of exposure, the pH level stabilizes, suggesting an equilibrium between cation exchange and apatite formation, which utilizes the OH^- ions present in the SBF [41,52]. The profiles of Ca, Si, P, and Mg ion release during immersion of MON-AKT composite scaffolds in SBF for 28 days are depicted in Fig. 7c. The concentration of P ions in the solution remained below 0.2 ppm for MON-AKT composite scaffolds, even after 28 days of immersion. The release of Ca ions gradually slowed down while, the release of Si and Mg ions gradually increased with prolonged soaking time. The interaction involving the substitution of H^+ with Ca^{2+} and Mg^{2+} from the SBF solution, coupled with the creation of silanol bonds (Si–OH) in the initial immersion periods, has been documented to elevate the OH^- concentration and elevate the solution's pH, facilitating apatite nucleation. As calcium, phosphate, and hydroxyl ions migrate toward the scaffold surface, resulting in the formation of bone-like apatite, the solution's pH experiences a gradual decline, signifying the utilization of hydroxyl ions in the apatite layer formation [41]. After 7 days of immersion, there is a noticeable decrease in phosphorus content, indicating rapid apatite formation during this period. The increasing trend in magnesium content confirms the resorbability of the prepared MON-AKT scaffold samples. Si ions released from the MON-AKT composite scaffold create Si–OH groups on the surface, altering the surface charge to negative and accelerating the deposition of Ca ions on the scaffold's surface [5]. Previous research suggests that the dissolution of Ca(II) ions from CaO–SiO glass produces silanol (Si–OH) groups on the surface, acting as nucleation sites for apatite [43]. Overall, the release of Ca from the MON-AKT composite scaffold enhances the concentration of Ca ions in the SBF solution. **Biodegradation** is a crucial aspect of synthetic materials designed for bone repair, as these materials should be capable of degrading as new bone tissue forms, facilitating bone tissue ingrowth and matrix deposition [46,50]. The degradation behavior of the MON-AKT composite scaffold, immersed in PBS solution for varying durations, is represented by the weight loss percentage (Fig. 7d). Notably, both the **weight loss** percentage and degradation rate of the MON-AKT composite scaffold exhibit a significant increase with prolonged immersion times. This phenomenon may be related to the finer-grained structure and enhanced interface formed between the samples and the solution, thereby stimulating the degradation rate of the specimens. A direct correlation between apatite formation ability and material degradability has been demonstrated [53]. Consequently, the increased content of bredigite and Si ions in the scaffolds leads to enhanced apatite formation ability and subsequently accelerate bone healing.

3.5. Antibacterial test and drug release

For the evaluation of antibacterial performance and drug release following AZT loading, MON-AKT composite scaffolds were chosen over other scaffolds due to their superior mechanical characteristics, higher bioactivity, and improved cytocompatibility. In this context, evaluating the antibacterial effectiveness of bone scaffolds is another key factor for treating bone infections, as it is essential for ensuring long-term therapeutic success [54–57]. Since pathogens like *S. aureus* can form biofilms within the bone, local antibiotic delivery is particularly valuable because it allows high drug concentrations to be delivered directly to the infection site [29]. AZT is a powerful macrolide antibiotic known for its effectiveness in treating severe infections [58]. It has been used to manage various acute bacterial infections, including those of the lungs, ears, and skin [59]. For bacteria to multiply, they rely on a specific protein synthesis process driven by ribosomal proteins. AZT controls various bacterial infections by blocking this process, specifically by inhibiting the transpeptidation/translocation phase and the assembly of the 5S ribosomal subunit [60]. This drug hinders bacterial survival and growth by causing a series of disruptions within them [21]. The FTIR spectrum of AZT shows a distinctive peak of the carbonyl group at 1735 cm^{-1} and a faint peak at 2972 cm^{-1} is attributed to the C–H group (Fig. 8a). A band at 1285 cm^{-1} is attributed to C–O–C and C–OH groups. Additionally, the absorption band at 3462 cm^{-1} is related to the O–H stretching vibrations [21,25,26,30]. The FTIR spectra of MON-AKT/AZT scaffolds display the distinctive peaks observed in the MON, AKT, and AZT scaffolds spectra. Fig. 8b illustrates the cumulative release of AZT over time from scaffolds loaded under different conditions. MON-AKT/1AZT scaffolds demonstrate the fastest and most pronounced release, while MON-AKT/2AZT scaffolds also achieve complete release within the first day, displaying a smoother release profile. Finally, MON-AKT/3AZT scaffolds exhibit a high initial release during the initial 10 h (57–60 %), followed by a sustained release for up to 24 h. At the experiment's conclusion, scaffolds were dissolved in solution, and the absorbance of solutions was recorded, confirming a complete release in 24 h for all MON-AKT scaffolds incorporating 1–3 % AZT (Fig. 8b). The substantial initial release of the drug from the scaffolds might be attributed to the drug's loose adhesion to the scaffold surfaces. Additionally, the more gradual release observed afterward could be due to the drug molecules being trapped within the microspores of the scaffold [61]. It is worth noting that MON-AKT/AZT scaffolds offer a notable advantage with their sustained drug release, a crucial feature for specific biomedical applications demanding prolonged therapeutic efficacy.

Olalde et al. [62] observed that Bioglass® scaffolds coated with PLGA containing vancomycin-loaded microgels deliver the drug quickly to provide antibacterial effects at the wound site, followed by a sustained release to support mid to long-term healing. Francis et al. [63] demonstrated that Bioglass® scaffolds coated with gentamycin exhibited a more rapid initial burst release than those coated with gentamycin-encapsulated polymer microspheres. Iviglia et al. [34] observed that HA/βTCP-Vancomycin scaffolds exhibited a significant burst release within 4–8 h. This rapid release occurs because vancomycin, being highly soluble, is not encapsulated or bound but merely adsorbed onto the ceramic surface. Consequently, when soaked in a physiological solution, the antibiotic is quickly released within a few hours.

For porous-based matrices, drug release is reported to be governed by diffusion, erosion/degradation, and swelling followed by diffusion. Despite some involvement of matrix degradation, under ideal sink conditions, the primary mechanism for drug delivery from mesoporous matrices is pore diffusion/convection, which could be modeled using first-order kinetics. Additional factors like drug-carrier and host-guest interactions play crucial roles in determining drug release profiles. Drug molecules can interact directly with the matrix, specifically the mesoporous material, with the microporosity of the scaffolds slowing their release. The processes of association and dissociation are presumed to be reversible. Typically, the reversible binding of a drug molecule to a carrier is believed to adhere to first-order kinetics. In this work, it is assumed that drug release patterns correspond to rapid diffusion/convection but slow association/dissociation. This results in the separation of drug association/dissociation from drug diffusion/convection processes: initially free drug molecules are released quickly through diffusion and convection, while the release of drug molecules that are initially bound occurs more slowly, governed by the dissociation process [64].

Additionally, the integration of AZT within MON-AKT scaffolds can significantly augment the antibacterial properties of MON-AKT scaffolds. Digital photos in Fig. 8c depict the antibacterial zones on agar plates at different culture times. MON-AKT, MON-AKT/1 to 3%AZT scaffolds were applied to the agar plates to inhibit bacterial growth.

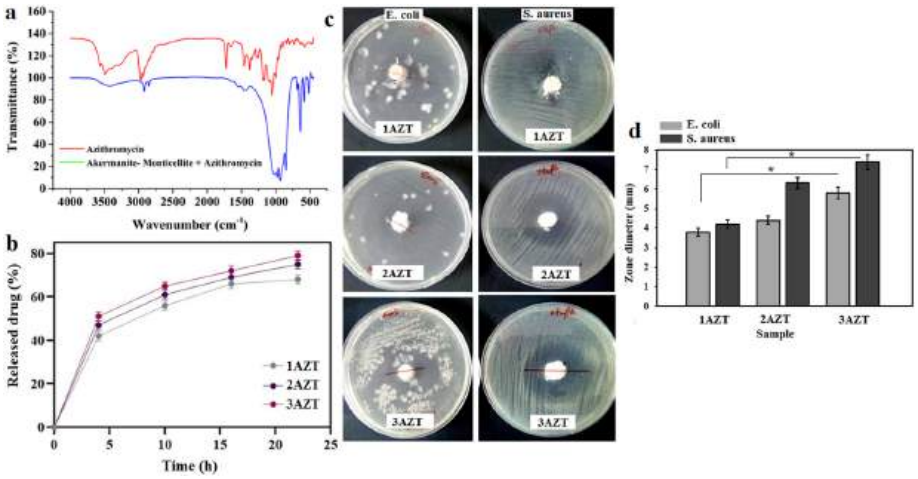

Fig. 8. (a) FTIR spectrum of azithromycin and MON-AKT/AZT scaffolds, (b) Pattern of drug release and the MON-AKT composite scaffold loaded with various amounts of AZT drug, (c) Images depicting the zones of inhibition, and (d) inhibition zone diameters against *E. coli* and *S. aureus* bacteria after 24 h (*$p < 0.05$).

Notably, both MON-AKT/3AZT and MON-AKT/2AZT nanocomposite scaffolds exhibited effective inhibition of bacterial growth, with zones of inhibition measuring 6.6 and 7.5 mm, respectively against S. aureus bacteria while this value is about 4.2 and 5.8 mm, respectively against E. coli bacteria. This suggests that MON-AKT/2-3AZT scaffolds possess significant antibacterial properties. In contrast, MON-AKT scaffolds with 1%AZT encapsulation showed less impediment to bacterial growth in both cases, indicating that the antibacterial effect is solely attributed to the encapsulated AZT drug. The incorporation of AZT into MON-AKT composite scaffolds led to a decline in the number of bacteria adhered to the scaffolds after 24 h of incubation, and this reduction occurred in a dose-dependent manner. Similar observations have been reported in other studies, suggesting a correlation with the mechanism of action of the antibiotic drug. AZT inhibits a crucial step in bacterial cell wall peptidoglycan synthesis, likely contributing to the observed antibacterial effects [26,30]. The results demonstrate that the inhibited bacterial growth zone against *E. coli* and *S. aureus* bacteria increases with the encapsulated AZT content in MON-AKT composite scaffolds. No significant difference in antibacterial performance was found between MON-AKT/1AZT and MON-AKT/3AZT scaffolds (*$p < 0.05$). The inhibition zone against *S. aureus* bacteria was larger compared to that for *E. coli* bacteria, likely due to structural and compositional differences. These findings suggest that the antibacterial efficacy of the scaffold is influenced by both the dopant AZT amount and the type of bacteria. Overall, MON-AKT/3AZT scaffolds exhibit a remarkably superior bacterial inhibition rate than other scaffold samples.

4. Conclusion

This research constitutes a thorough exploration into the fabrication of highly porous MON-AKT composite scaffolds, both with and without the incorporation of AZT. The experimental findings highlight that the addition of AKT to MON-based composite scaffolds leads to more refined crystal structures and higher mechanical strength compared to the monolithic MON and AKT scaffold samples. The composite scaffolds exhibit superior apatite formation and bioactivity compared to their pure counterparts. In terms of biological response, MON-AKT composite scaffolds demonstrate enhanced cell viability, cell attachment, and significant osteogenic differentiation with high ALP activity. MON-AKT composite scaffolds containing AZT are successfully immobilized on the pore walls, showcasing prolonged drug release with an initial burst release within 10 h, followed by sustained delivery over 24 h. The antimicrobial properties indicate that AZT released from the systems effectively inhibits the growth of S. aureus and E. coli bacteria. Overall, the results suggest that MON-AKT composite scaffolds with AZT hold great potential for bone tissue regeneration and preventing post-operative infections.

Abbreviations

AKT	Akermanite	MA	Mechanical activation
ALP	Alkaline phosphatase	MER	Merwinite
ATCC	American Type Culture Collection	MON	Monticellite
AZT	Azithromycin	MTT	3-(4,5-dimethylthiazol-2-yl)-2,5-diphenyltetrazolium bromide
BTE	Bone tissue engineering	nm	Nanometer
CSB	Calcium silicate-based bioceramic	PBS	Phosphate-buffered saline
DI	Deionized	SBF	Simulated body fluid
DIO	Diopside	SEM	Scanning electron microscopy
EDS	Energy-dispersive X-ray spectroscopy	TEM	Transmission electron microscopy
FTIR	Fourier-transform infrared spectroscopy	TEOS	Tetraethyl orthosilicate
HAp	Hydroxyapatite	UV	Ultraviolet
ICP	Inductively coupled plasma	XRD	X-ray diffraction

CRediT authorship contribution statement

M. Assarzadehgan: Supervision, Writing – review & editing, Conceptualization, Data curation, Formal analysis. **Ibrahim Saeed Gataa:** Writing – review & editing, Conceptualization, Data curation, Formal analysis. **Zainab Younus Abdullah:** Investigation, Writing – original draft. **M. Kasiri-Asgarani:** Formal analysis, Writing – original draft. **A. Najafinezhad:** Writing – review & editing, Conceptualization, Data curation, Formal analysis. **H.R. Bakhsheshi-Rad:** Supervision, Writing – review & editing. **M. Razzaghi:** Supervision, Writing – review & editing, Conceptualization. **Soheil Salahshour:** Investigation, Writing – original draft. **D. Toghraie:** Conceptualization, Data curation, Formal analysis.

Declaration of competing interest

The authors declare that they have no known competing financial interests or personal relationships that could have appeared to influence the work reported in this paper.

Appendix

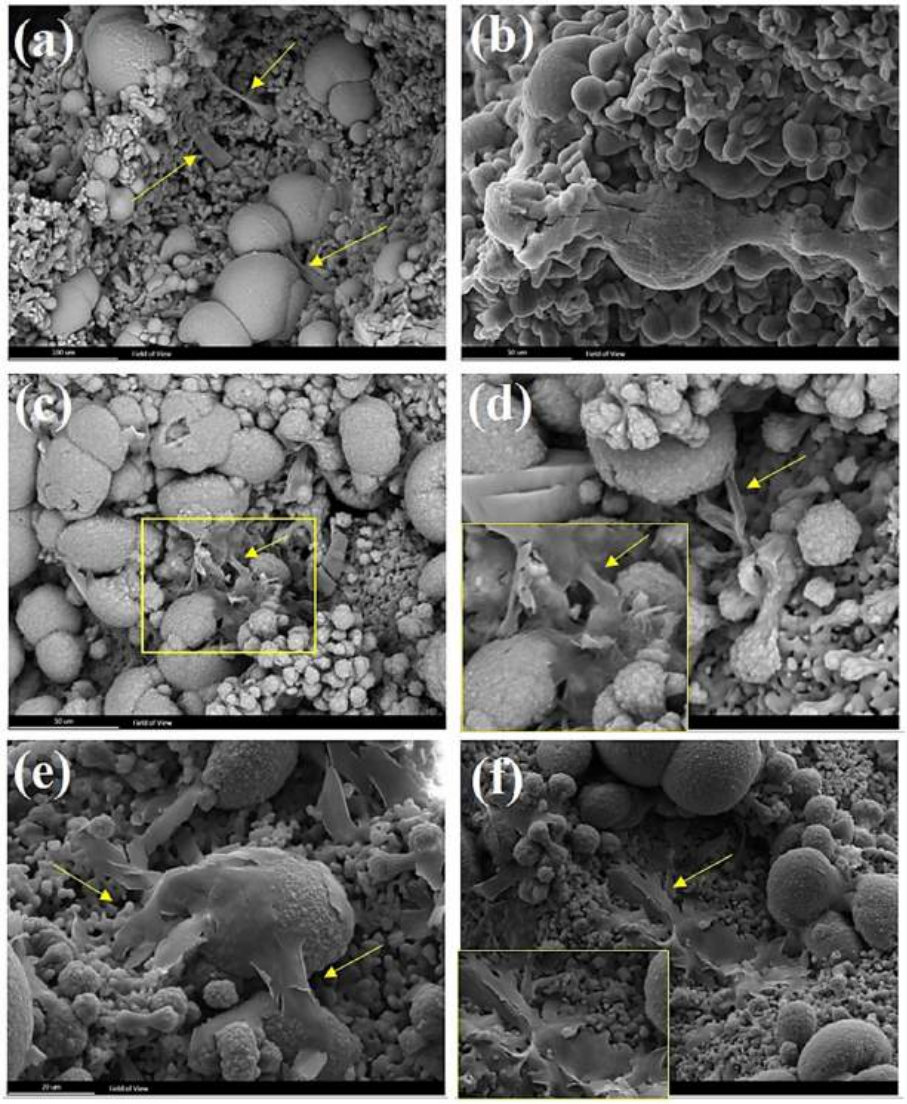

Fig. A1. SEM images of the morphology and adhesion of MG63 osteoblast cells for (a-b) MON scaffold, (d-f) AKT scaffold and (g-i) MON-AKT composite scaffold sample.

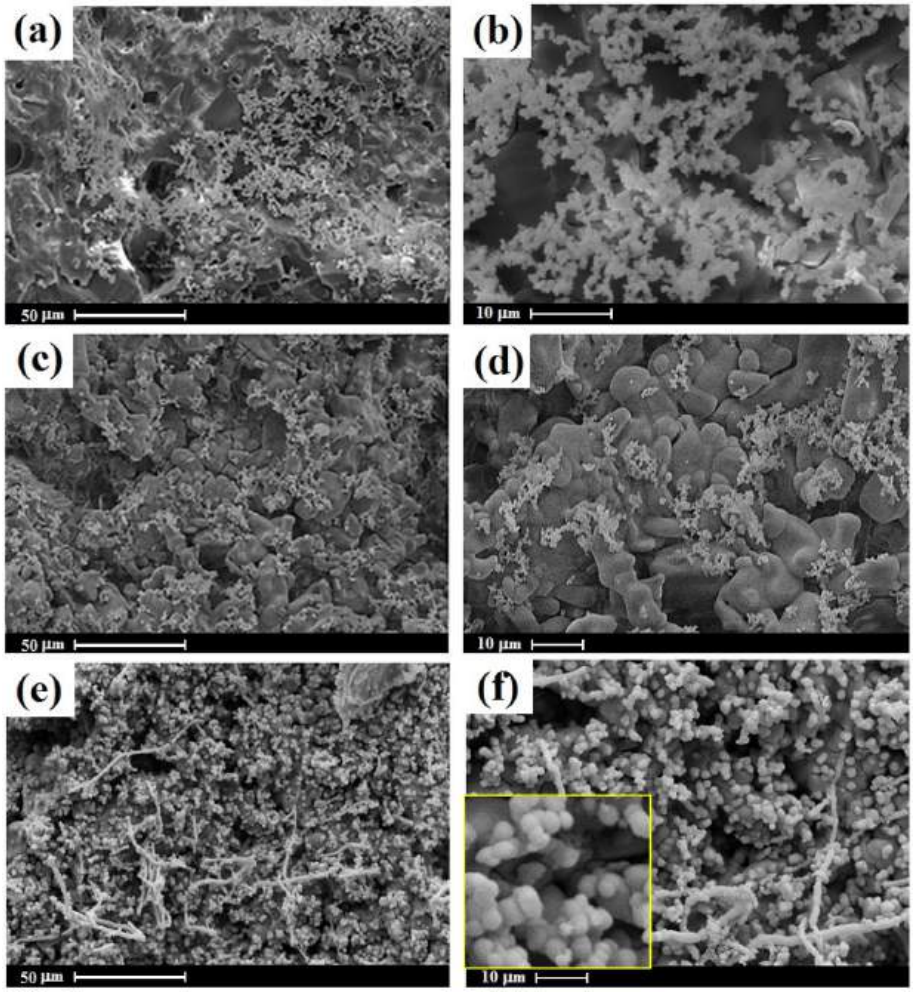

Fig. A2. SEM images of high magnification of (a,b) MON scaffolds, (c,d) AKT scaffold, and (e,f) MON-AKT composite scaffold after 28 days of immersion in SBF.

References

[1] S. Sadreddini, et al., Novel barium-doped-baghdadite incorporated PHBV-PCL composite fibrous scaffolds for bone tissue engineering, J. Mech. Behav. Biomed. Mater. 148 (2023) 106185.
[2] M. Mirkhalaf, et al., Personalized 3D printed bone scaffolds: a review, Acta Biomater. 156 (2023) 110–124.
[3] C. Chen, et al., Targeting calcium magnesium silicates for polycaprolactone/ ceramic composite scaffolds, ACS Biomater. Sci. Eng. 1 (2) (2015) 94–102.
[4] S. Wang, et al., Encapsulation of amoxicillin within laponite-doped poly(lactic-co-glycolic acid) nanofibers: preparation, characterization, and antibacterial activity, ACS Appl. Mater. Interfaces 4 (11) (2012) 6393–6401.
[5] H. Jodati, et al., 3D porous bioceramic based boron-doped hydroxyapatite/ baghdadite composite scaffolds for bone tissue engineering, J. Mech. Behav. Biomed. Mater. 140 (2023) 105722.
[6] S. Mehrafzoon, S.A. Hassanzadeh-Tabrizi, A. Bigham, Synthesis of nanoporous Baghdadite by a modified sol-gel method and its structural and controlled release properties, Ceram. Int. 44 (12) (2018) 13951–13958.
[7] X. Wang, et al., 45S5 Bioglass analogue reinforced akermanite ceramic favorable for additive manufacturing mechanically strong scaffolds, RSC Adv. 5 (124) (2015) 102727–102735.
[8] H.R. Bakhsheshi-Rad, et al., Coating biodegradable magnesium alloys with electrospun poly-L-lactic acid-åkermanite-doxycycline nanofibers for enhanced biocompatibility, antibacterial activity, and corrosion resistance, Surf. Coating. Technol. 377 (2019) 124898.
[9] A. Bigham, et al., A 3D nanostructured calcium-aluminum-silicate scaffold with hierarchical meso-macroporosity for bone tissue regeneration: fabrication, sintering behavior, surface modification and in vitro studies, J. Eur. Ceram. Soc. 41 (1) (2021) 941–962.
[10] P. Zadehnajar, et al., Recent advances on akermanite calcium-silicate ceramic for biomedical applications, Int. J. Appl. Ceram. Technol. 18 (6) (2021) 1901–1920.
[11] M. Diba, et al., Magnesium-containing bioactive polycrystalline silicate-based ceramics and glass-ceramics for biomedical applications, Curr. Opin. Solid State Mater. Sci. 18 (3) (2014) 147–167.
[12] E. Kalantari, et al., Nanostructured monticellite for tissue engineering applications - Part I: microstructural and physicochemical characteristics, Ceram. Int. 44 (11) (2018) 12731–12738.
[13] H.R. Bakhsheshi-Rad, et al., Synthesis and in-vitro performance of nanostructured monticellite coating on magnesium alloy for biomedical applications, J. Alloys Compd. 773 (2019) 180–193.
[14] M. Rahmati, M. Fathi, M. Ahmadian, Preparation and structural characterization of bioactive bredigite (Ca7MgSi4O16) nanopowder, J. Alloys Compd. 732 (2018) 9–15.
[15] L. Koroglu, et al., A novel approach for synthesis of monticellite based bioactive ceramic powders from boron derivative waste, Mater. Lett. 209 (2017) 315–318.
[16] P. Kaur, et al., Sol-gel derived strontium-doped SiO_2–CaO–MgO–P_2O_5 bioceramics for faster growth of bone like hydroxyapatite and their in vitro study for orthopedic applications, Mater. Chem. Phys. 245 (2020) 122763.
[17] N. Namvar, et al., Toward reducing the formation temperature of diopside via wet-chemical synthesis routes using chloride precursors, Ceram. Int. 43 (16) (2017) 13781–13785.
[18] E. Askari, et al., A hybrid approach for in-situ synthesis of bioceramic nanocomposites to adjust the physicochemical and biological characteristics, J. Mater. Res. Technol. 14 (2021) 464–474.
[19] M.S. Collin, et al., Solution combustion synthesis of functional diopside, akermanite, and merwinite bioceramics: excellent biomineralization, mechanical strength, and antibacterial ability, Mater. Today Commun. 27 (2021) 102365.
[20] H. Mohammadi, et al., Structural, physicomechanical, and in vitro biodegradation studies on Sr-doped bioactive ceramic, Ceram. Int. 45 (11) (2019) 14090–14097.
[21] S. Jafari, et al., An azithromycin electrochemical sensor based on an aniline MIP film electropolymerized on a gold nano urchins/graphene oxide modified glassy carbon electrode, J. Electroanal. Chem. 829 (2018) 27–34.

[22] M. Myat-Htun, et al., Enhanced sinterability and in vitro bioactivity of barium-doped akermanite ceramic, Ceram. Int. 46 (11) (2020) 19062–19068. Part B.
[23] Á. Serrano-Aroca, et al., Scaffolds in the microbial resistant era: fabrication, materials, properties and tissue engineering applications, Materials Today Bio 16 (2022) 100412.
[24] H.R. Bakhsheshi-Rad, et al., Synthesis of novel nanostructured bredigite–amoxicillin scaffolds for bone defect treatment: cytocompatibility and antibacterial activity, J. Sol. Gel Sci. Technol. 86 (1) (2018) 83–93.
[25] B.P. Upoma, et al., A fast adsorption of azithromycin on waste-product-derived graphene oxide induced by H-bonding and electrostatic interactions, ACS Omega 7 (34) (2022) 29655–29665.
[26] K. Zhang, et al., Facile synthesis of the necklace-like graphene oxide-multi-walled carbon nanotube nanohybrid and its application in electrochemical sensing of Azithromycin, Anal. Chim. Acta 787 (2013) 50–56.
[27] S.M. Dizaj, et al., Antimicrobial activity of the metals and metal oxide nanoparticles, Mater. Sci. Eng. C 44 (2014) 278–284.
[28] J. Chen, et al., 3D printing for bone repair: coupling infection therapy and defect regeneration, Chem. Eng. J. 471 (2023) 144537.
[29] M. Parent, et al., Hydroxyapatite microporous bioceramics as vancomycin reservoir: antibacterial efficiency and biocompatibility investigation, J. Biomater. Appl. 31 (4) (2016) 488–498.
[30] S. Huo, et al., Graphene oxide with acid-activated bacterial membrane anchoring for improving synergistic antibacterial performances, Appl. Surf. Sci. 551 (2021) 149444.
[31] J. Ma, et al., In vitro degradability and apatite-formation ability of monticellite (CaMgSiO4) bioceramic, Ceram. Int. 45 (3) (2019) 3754–3759.
[32] T. Kokubo, H. Takadama, How useful is SBF in predicting in vivo bone bioactivity? Biomaterials 27 (15) (2006) 2907–2915.
[33] M.-q. Cheng, et al., A novel open-porous magnesium scaffold with controllable microstructures and properties for bone regeneration, Sci. Rep. 6 (1) (2016) 24134.
[34] G. Iviglia, et al., Engineered porous scaffolds for periprosthetic infection prevention, Mater. Sci. Eng. C 68 (2016) 701–715.
[35] H.R. Bakhsheshi-Rad, et al., A new multifunctional monticellite-ciprofloxacin scaffold: preparation, bioactivity, biocompatibility, and antibacterial properties, Mater. Chem. Phys. 222 (2019) 118–131.
[36] G.H. Yang, et al., Investigating the physical characteristics and cellular interplay on 3D-printed scaffolds depending on the incorporated silica size for hard tissue regeneration, Mater. Des. 207 (2021) 109866.
[37] E. Askari, et al., Highly bioactive Akermanite-Monticellite nanocomposites for bone tissue engineering: a tunable three-dimensional biological study, J. Mater. Res. Technol. 20 (2022) 4066–4076.
[38] P. Srinath, et al., A novel cost-effective approach to fabricate diopside bioceramics: a promising ceramics for orthopedic applications, Adv. Powder Technol. 32 (3) (2021) 875–884.
[39] G.A. Nasser Atia, et al., Baghdadite: a novel and promising calcium silicate in regenerative dentistry and medicine, ACS Omega 7 (49) (2022) 44532–44541.
[40] S. Ramezani, et al., Synthesis, characterization and in vitro behavior of nanostructured diopside/biphasic calcium phosphate scaffolds, Mater. Chem. Phys. 186 (2017) 415–425.
[41] M. Eilbagi, et al., Mechanical and cytotoxicity evaluation of nanostructured hydroxyapatite-bredigite scaffolds for bone regeneration, Mater. Sci. Eng. C 68 (2016) 603–612.
[42] J.C. Knowles, S. Talal, J.D. Santos, Sintering effects in a glass reinforced hydroxyapatite, Biomaterials 17 (14) (1996) 1437–1442.
[43] A. Najafinezhad, et al., On the synthesis of nanostructured akermanite scaffolds via space holder method: the effect of the spacer size on the porosity and mechanical properties, J. Mech. Behav. Biomed. Mater. 69 (2017) 242–248.
[44] H.-W. Kim, et al., Effect of CaF2 on densification and properties of hydroxyapatite–zirconia composites for biomedical applications, Biomaterials 23 (20) (2002) 4113–4121.
[45] M.R. Shahrouzifar, E. Salahinejad, Strontium doping into diopside tissue engineering scaffolds, Ceram. Int. 45 (8) (2019) 10176–10181.
[46] H. Mohammadi, et al., Effect of strontium substitution on structural, sinterability, physicomechanical and biological properties of akermanite ceramic, J. Mech. Behav. Biomed. Mater. 116 (2021) 104379.
[47] M.M. Costa, et al., Development of β-TCP-Ti6Al4V structures: driving cellular response by modulating physical and chemical properties, Mater. Sci. Eng. C 98 (2019) 705–716.
[48] E. Kalantari, et al., Biocomposites based on hydroxyapatite matrix reinforced with nanostructured monticellite (CaMgSiO4) for biomedical application: synthesis, characterization, and biological studies, Mater. Sci. Eng. C 105 (2019) 109912.
[49] S. Yadav, et al., In-vitro analysis of bioactivity, hemolysis, and mechanical properties of Zn substituted Calcium Zirconium silicate (baghdadite), Ceram. Int. 47 (11) (2021) 16037–16053.
[50] M. Díaz-Pérez, et al., CaO–MgO–SiO_2–P_2O_5- based multiphase bio-ceramics fabricated by directional solidification: microstructure features and in vitro bioactivity studies, Ceram. Int. 47 (12) (2021) 17041–17048.
[51] S.K. Venkatraman, et al., Comparative investigation on antibacterial, biological and mechanical behaviour of monticellite and diopside derived from biowaste for bone regeneration, Mater. Chem. Phys. 286 (2022) 126157.
[52] R. Keihan, et al., Biomineralization, strength and cytocompatibility improvement of bredigite scaffolds through doping/coating, Ceram. Int. 46 (13) (2020) 21056–21063.
[53] P. Ducheyne, S. Radin, L. King, The effect of calcium phosphate ceramic composition and structure on in vitro behavior. I. Dissolution, J. Biomed. Mater. Res. 27 (1) (1993) 25–34.
[54] H.R. Bakhsheshi-Rad, A.F. Ismail, M. Aziz, Z. Hadisi, M. Omidi, X. Chen, Antibacterial activity and corrosion resistance of Ta_2O_5 thin film and electrospun PCL/MgO-Ag nanofiber coatings on biodegradable Mg alloy implants, Ceram. Int. 45 (9) (2019) 11883–11892.
[55] H.R. Bakhsheshi-Rad, E. Hamzah, A.F. Ismail, M. Aziz, M. Kasiri-Asgarani, E. Akbari, S. Jabbarzare, A. Najafinezhad, Z. Hadisi, Synthesis of a novel nanostructured zinc oxide/baghdadite coating on Mg alloy for biomedical application: in-vitro degradation behavior and antibacterial activities, Ceram. Int. 43 (17) (2017) 14842–14850.
[56] M.M. Salim, N.A. Malek, Characterization and antibacterial activity of silver exchanged regenerated NaY zeolite from surfactant-modified NaY zeolite, Mater. Sci. Eng. C 59 (2016) 70–77.
[57] F. Zheng, S. Wang, S. Wen, M. Shen, M. Zhu, X. Shi, Characterization and antibacterial activity of amoxicillin-loaded electrospun nano-hydroxyapatite/poly (lactic-co-glycolic acid) composite nanofibers, Biomaterials 34 (4) (2013) 1402–1412.
[58] B. Nigovic, Adsorptive stripping voltammetric determination of azithromycin at a glassy carbon electrode modified by electrochemical oxidation, Anal. Sci. 20 (4) (2004) 639–643.
[59] M.J. Parnham, V.E. Haber, E.J. Giamarellos-Bourboulis, G. Perletti, G.M. Verleden, R. Vos, Azithromycin: mechanisms of action and their relevance for clinical applications, Pharmacology & therapeutics 143 (2) (2014) 225–245.
[60] R. Mostafazadeh, H. Karimi-Maleh, A. Ghaffarinejad, F. Tajabadi, Y. Hamidian, Highly sensitive electrochemical sensor based on carbon paste electrode modified with graphene nanoribbon–$CoFe_2O_4$@ NiO and ionic liquid for azithromycin antibiotic monitoring in biological and pharmaceutical samples, Appl. Nanosci. 13 (9) (2023) 5829–5838.
[61] W. Li, Y. Ding, R. Rai, J.A. Roether, D.W. Schubert, A.R. Boccaccini, Preparation and characterization of PHBV microsphere/45S5 bioactive glass composite scaffolds with vancomycin releasing function, Mater. Sci. Eng. C 41 (2014) 320–328.
[62] B. Olalde, N. Garmendia, V. Sáez-Martínez, N. Argarate, P. Nooeaid, F. Morin, A. R. Boccaccini, Multifunctional bioactive glass scaffolds coated with layers of poly (d, l-lactide-co-glycolide) and poly (n-isopropylacrylamide-co-acrylic acid) microgels loaded with vancomycin, Mater. Sci. Eng. C 33 (7) (2013) 3760–3767.
[63] L. Francis, D. Meng, J.C. Knowles, I. Roy, A.R. Boccaccini, Multi-functional P (3HB) microsphere/45S5 Bioglass®-based composite scaffolds for bone tissue engineering, Acta Biomater. 6 (7) (2010) 2773–2786.
[64] R. García-Alvarez, I. Izquierdo-Barba, M. Vallet-Regí, 3D scaffold with effective multidrug sequential release against bacteria biofilm, Acta Biomater. 49 (2017) 113–126.